Nanoscale

PAPER

View Article Online
View Journal | View Issue

Cite this: *Nanoscale*, 2025, **17**, 7076

Densely distributed Co onto carbon-layer-coated flower-like Ni/Al_2O_3 and its tailored integration into a stirrer for multiple catalytic degradation and solar-powered water evaporation†

Shuang Jiang,‡[a] Hongyao Zhao,‡[a] Zichen Ma,[a] Hongyang Zhu,[a] Danhong Shang,[a] Linzhi Zhai,[a] Yanyun Wang,*[a] Yiyan Song*[a,b] and Fu Yang *[a]

Multiple functional tailored materials have shown great potential for both pollutant degradation and freshwater recovery. In this study, we synthesized densely distributed Co onto carbon-layer-coated Ni/Al_2O_3 hydrangea composites (Ni/Al_2O_3@Co) *via* the polymerization of dopamine under a controlled graphitized process. The characterization results revealed that Ni/Al_2O_3@Co, with abundant exposed bimetallic Co–Ni species on the surface of Al_2O_3, could afford accessible catalytic sites for persulphate activation and subsequent pollutant degradation. The tetracycline (TC) degradation rate of optimal Ni/Al_2O_3@Co_{500} reached 98.1% within 15 min with a first-order rate constant of 0.498 min^{-1}, which is ~1.38 times that of Al_2O_3@Co_{500} (0.362 min^{-1}), indicating the existing Co–Ni intermetallic synergy. Free radical quenching experiments indicated that $^{\bullet}O_2^-$ plays a leading role in the catalytic degradation of TC. Moreover, Ni/Al_2O_3@Co_{500} afforded strong flexibility for the degradation of methylene blue (MB), norfloxacin (NFX), bisphenol A (BPA), and oxytetramycin (OTC). Ni/Al_2O_3@Co_{500} catalysts were anchored onto a customized sponge *via* a calcium-triggered hydrogel crosslink strategy to construct an integral and tailored stirrer, which was used directly as the mechanical stirrer catalyst for the activation of peroxymonosulfate and pollutant removal. This obtained stirrer was also used as a monolith evaporator affording an evaporation rate of 1.944 kg m^{-2} h^{-1} at a solar-driven photothermal interface. We also demonstrated that the shape of the tailored sponge weakly affects the course of the degradation reaction. Furthermore, the degradation rates of TC in actual water sources on a Ni/Al_2O_3@Co_{500} sponge were still maintained up to 90% with rational recycling properties, which provide a promising solution for the multiple-functional pollutant degradation and water regeneration.

Received 26th October 2024,
Accepted 5th December 2024

DOI: 10.1039/d4nr04430d

rsc.li/nanoscale

1. Introduction

With the rapid development of industry and human society, various emerging contaminants have been found in water bodies, which pose irreversible threats to humans. In particular, tetracycline (TC), a broad-spectrum antibiotic, has been widely used in medicine and animal husbandry.[1] Due to the uncontrolled discharge of medical sewage and poultry manure, a large number of natural water bodies are contaminated with residual TC, leading to increased multi-drug resistance and pathogenicity of bacteria. More seriously, TC is difficult to degrade naturally, and the accumulated TC and its derivatives pose a huge threat to the ecological environment and human health.[2] Therefore, the treatment of wastewater containing these contaminants raises concerns to the industry and researchers; furthermore, the continuous regeneration of cleanwater from wastewater has become extremely challenging.

Nowadays, various approaches such as adsorption, biodegradation, and advanced oxidation processes (AOPs) have been widely investigated for TC elimination.[3] Among these, AOPs have shown huge potential in wastewater treatment. The focus of AOPs lies in the generation of highly reactive oxygen species (ROS) from various peroxides, which can attack most

[a]*School of Environmental and Chemical Engineering, Jiangsu University of Science and Technology, Zhenjiang 212003, China. E-mail: fuyang@just.edu.cn, wangyanyun@just.edi.cn*
[b]*Department of Clinical Laboratory, The Fifth People's Hospital of Suzhou, The Affiliated Infectious Diseases Hospital of Soochow University, Suzhou, 215000, China. E-mail: songyiyan94@163.com*

†Electronic supplementary information (ESI) available. See DOI: https://doi.org/10.1039/d4nr04430d

‡These author equally contributed to this work.

organic pollutants and degrade them into harmless products, such as carbon dioxide and water. The AOPs involving peroxymonosulfate (PMS) activation have attracted widespread attention from researchers;[4] particularly, the asymmetrical PMS molecule structure with easy O–O bond breakage is readily activated by various catalysts.[5,6] Moreover, AOPs occurring in a confined space shorten the distance between the ROS generated at the active site and organic pollutants, thereby improving the utilization of ROS and catalytic efficiency.[7] Thus, this approach provides many effective solutions for the removal of refractory and complex organic pollutants.

Despite significant progress in AOPs, some challenges and difficulties exist when it comes to the design and construction of metal catalysts. Transition metal catalysts have received considerable attention in PMS activation,[8,9] wherein metals with various oxidation states can often act as electron transfer mediators in the redox reactions and provide or accept electrons to promote the reaction.[10,11] Among transition metals, Co-based catalysts are known for their high activity in the activation of the PMS molecule, affording excellent catalytic degradation efficiency.[12] However, nanometric metal species often require more protection of support to stabilize these existing highly active metal nanoparticles. To the best of our knowledge, alumina-based Al_2O_3 is widely used as a stable catalyst support, which can well disperse these metal nanoparticles and inhibit their aggregation.[13] However, Al_2O_3 is usually difficult to further optimize the reaction efficiency of existing metal species *via* electron structure modification, so researchers tried to introduce additional substances to improve the catalytic properties of loaded metals. For instance, Wu and co-workers[14] designed an alumina-supported iron (Fe-Al_2O_3) catalyst in which Fe is dissolved in the Al_2O_3 collective and, using SiO_2 promotes the catalytic growth of carbon nanotubes. Xie *et al.*[15] prepared a new nanocomposite of Co-doped Al_2O_3 nanoparticle-supported Pt nanoparticles (Pt/Co-Al_2O_3), exhibiting good catalytic durability and photothermal conversion. This inspires us to construct multiple metal-loaded synergetic catalysts for PMS activation and pollutant degradation.

Although metal-carrier interaction plays an important role, the catalytic performance of bimetallic catalysts is affected by many factors including structure, composition, and shape. Alloying metals can induce structural and electronic changes in the active metal, thereby improving the dispersion, sintering resistance, and adsorption properties of the metal.[16] Constructing the synergistic effect of multiple metals to improve the limited inherent activity of one or two metals may be an effective method to achieve coupling of electronic interaction and improve the reactivity of two metals. In addition, ensuring enough interaction of metal species to trigger rational synergetic effects is a challenge. Our groups developed the polydopamine modification strategy which could introduce additional metals onto the support and ensure their dispersion on the support. However, the coupling effect between these matched metals has not been explored in the following application.

As mentioned in the above discussion, in addition to the removal of pollutants from wastewater, the direct regeneration of clean water from wastewater is a major focus of environmental governance. In recent years, the utilization of green solar energy for water evaporation has been a research hotspot of water resource regeneration.[17] For example, Zhou[18] group prepared a solar evaporator with a hydrophilic polyacrylamide/carbon nanotube as a raw material modified with perfluorooctane trichlorosilane, owing to excellent water evaporation rate and photothermal conversion efficiency. Tessema *et al.*[19] also used electrospinning technology to develop non-porous hydrophobic fiber membranes for seawater desalination. The evaporator has good performance in photothermal conversion, sewage treatment, and desalting. However, these developed evaporators often show limited functionality in the wastewater. It has been found that the combination of catalytic metal substances with photothermal conversion properties can not only drive interfacial water evaporation *via* solar energy[20] but also improve the catalytic performance of the catalyst under natural light irradiation as a photothermal catalyst, which plays an important role in environmental governance.

Inspired by these ideas, we synthesized Ni and Co co-modified carbon-coated Al_2O_3 composites *via* the polymerization of dopamine under different temperature treatments to obtain the multiple metallic integrated synergetic hydrangea-like nanocatalyst. It is worth noting that, with the assistance of the carbon protection layer, more metal nanoparticles can be stabilized onto the nanosheet of nanohydrangea, and the densely dispersed metal nanoparticle spontaneously assembled on the support during the pyrolysis process. Various characterizations will be performed to determine the physicochemical properties of the catalysts. Afterward, the catalytic degradation performance of TC over these compara-

Fu Yang

Professor Fu Yang received his PhD in Industrial Catalysis from Nanjing Tech University in 2018. He is currently a Full Professor and the Head of the Energy and Chemical Engineering major in Jiangsu University of Science and Technology. He was awarded the title of Young Outstanding Scientist of Jiangsu Low Carbon Technology Society in 2019 and the Journal of Materials Chemistry's A Emerging Scientist. His research interest is mainly focused on the national important needs of fine chemical synthesis, energy molecule conversion, environmental governance, etc. *He has published more than 120 SCI academic papers in important internationally renowned journals in Chemistry, Engineering, Materials and Environment.*

tive catalysts obtained under different temperature treatments will be investigated to select the best catalysts. The related catalytic mechanisms for PMS activation and generation of reactive oxidative species and interference experiments will also be studied. To evaluate the catalytic performance under sunlight, we further integrated the catalyst onto the tailored sponge with different shapes to form an integrated monolith photothermal material. An assay was performed to investigate whether the photothermal material affects the degradation of pollutants in the water sources. The photothermal material was tested for its photothermal conversion and water evaporation ability under the simulated solar light. It is hoped that this will provide new solutions to solve the problem of wastewater and clean water regeneration.

2. Experimental section

2.1. Materials and reagents

Aluminum nitrate ($Al(NO)_3{\cdot}9H_2O$, AR), polyvinylpyrrolidone (k30, PVP), tris(hydroxymethyl)aminomethane ($C_4H_{11}NO_3$), ethanol (EtOH), acetone (C_3H_6O), nickelous nitrate ($Ni(NO_3)_2$), hydrochloric acid (HCl), hydrochloric dopamine ($C_8H_{12}ClNO_2$), cobalt acetate tetrahydrate ($Co(CH_3COO)_2{\cdot}4H_2O$), methanol (99.9%, CH_3OH), *tert*-butanol (99.5%, $C_4H_{10}O$), L-histidine (99%, $C_6H_9N_3O_2$), and *p*-benzoquinone (98%, $C_6H_4O_2$) were achieved from Energy Co., Ltd. Sodium chloride (99.7%, NaCl), Sodium carbonate (Na_2CO_3, AR), Sodium bicarbonate (99.5%, $NaHCO_3$), Sodium sulphate (99.5%, Na_2SO_4) and Sodium hydroxide (NaOH, AR) were obtained from Shanghai Aladdin Industrial Co. LTD. Tetracycline (TC, CP, $C_{22}H_{24}N_2O_8$) and oxytetracycline (OTC, 98%, $C_{22}H_{24}N_2O_9$) were purchased from Shanghai Macklin Biochemical Technology Co., Ltd. Bisphenol A (BPA, AR) and potassium peroxymonosulfate complex salt (PMS) were purchased from Energy Co., Ltd. Methylene blue (MB, AR) was obtained from Nanjing reagent Co., Ltd. Norfloxacin (NFX, AR) was purchased from Adamas Reagent Co., Ltd. All the chemicals were used without further purification.

2.2. Synthesis of Ni-doped hydrangea-shaped materials

First, Ni-doped hydrangea-shaped AlOOH was prepared by a hydrothermal method. Then $Al(NO)_3{\cdot}9H_2O$ (0.520 g) was dissolved in 20 ml of deionized water, followed by the addition of 20 ml of ethanol containing PVP (0.520 g). After mixing these two solutions, 10 ml of acetone and 300 ml of 0.5 mol L^{-1} Ni $(NO_3)_2$ solution were introduced later. Then the prepared mixture was transferred into a PTFE hydrothermal reactor incubated at 180 °C for 24 h. After cooling to room temperature, the product was obtained and washed three times with deionized water and ethanol, respectively. Afterward, the resulting sample was dried in an oven at 70 °C for 24 h. The obtained samples were denoted as AlOOH-Ni. In contrast, the comparative sample AlOOH was obtained following the same synthetic procedure as mentioned above without the addition of Ni precursor.

2.3. Synthesis of Co-modified catalysts

Tris(hydroxymethyl)aminomethane was evenly dispersed in 12 ml 0.2 mol L^{-1} hydrochloric acid to obtain a buffer solution. Then the obtained AlOOH-Ni (0.5 g) was added to a 70 ml buffer solution for 20 min sonication. Subsequently, hydrochloric dopamine (0.5 g) was added to the above-mentioned dark green solution to obtain a black solution. Cobalt acetate tetrahydrate (1 mmol) was dissolved into a spot of ethanol and poured into the afore-acquired black solution. After stirring continuously for 24 h, the product was washed with deionized water and ethanol and then dried at 70 °C for 24 h. The dried sample was placed in a tubular furnace under an N_2 atmosphere for calcination at temperatures of 400, 500, and 600 °C for 3 h at a heating rate of 2 °C min^{-1}, respectively. The corresponding samples were labeled as $Ni/Al_2O_3@Co_{400}$, $Ni/Al_2O_3@Co_{500}$, and $Ni/Al_2O_3@Co_{600}$, respectively. In contrast, AlOOH-Ni was replaced with AlOOH for the same operation at a temperature of 500 °C to obtain Al_2O_3@Co. The samples were synthesized only without adding Co precursors and labeled as Ni/Al_2O_{3-500}.

2.4. Characterizations

The surface morphology and elemental composition of the prepared materials were observed using a scanning electron microscope (SEM) (S4800, Japan). Transmission electron microscopic (TEM) images were acquired using a JEM-2010 EX microscope (JEOL, Tokyo, Japan) equipped with EDX. Raman spectra were recorded at room temperature using a Spex 1877D triplemate spectrograph with 2 cm^{-1} resolution. The X-ray photoelectron spectra (XPS) were recorded using a PHI 5000 Versa Probe X-ray photoelectron spectrometer (ULVAC-PHI, Kanagawa, Japan) equipped with Al Kα radiation (1486.6 eV). The C 1s peak at 284.6 eV was used as the reference for binding energies. Phase structure analysis of various samples was performed using an X-ray diffractometer (XRD-6000X, Shimadzu Corporation, Tokyo, Japan) with Cu Kα radiation (λ = 1.54178 Å). The open circuit voltage (OCV), cyclic voltammetry (CV), and electrochemical impedance spectra (EIS) analyses were performed using a CHI760E electrochemical workstation by a standard three-electrode method. In this setup, a platinum electrode served as the counter electrode, and an Ag/AgCl electrode was used as the reference electrode. A solar simulator, a 360° optical path converter, and an infrared thermal imager were used to acquire the infrared images of the materials under simulated sunlight. The photothermal conversion ability of the materials was determined. The photothermal imaging of the comparative samples was performed on a polymer membrane placed on dust-free paper dipped in water using a UTi260B thermal imager (UNIT by Yulide Technology (China) Co, LTD), and a sunlight solar simulator (Solar 500 T, Beijing Newbit Technology) was operated to provide one stimulated sunlight. The total organic carbon (TOC) was determined using an LB-T5000 total organic carbon analyzer.

2.5. Catalytic performance evaluation

Successive TC degradation experiments using PMS as an oxidant were conducted in a 50 ml beaker, and the reaction

dynamic courses were recorded using a UV spectrophotometer (MAPADA P1800) to evaluate the performance of the catalyst for the catalytic degradation of TC. Briefly, 20 mg of PMS was added to 0.2 g L^{-1} of TC solution under stirring. Subsequently, 20 mg of catalyst was added to the solution and the catalyst was allowed to absorb the contaminants. At certain time intervals, 2–3 ml of the solution was removed for measurement. The initial solution was used as a blank control. Other pollutant degradation can refer to the above-mentioned operation procedures.

The reusability of the catalyst for TC degradation was assessed as follows. The catalyst obtained from the previous cycle was collected by magnetic separation, washed with ethanol and water, respectively, and then dried at 70 °C. Subsequently, the collected catalyst was burned in a tubular furnace at 200 °C for 2 h to remove the residual pollutants. In the next cycle, the regenerated catalyst was re-dispersed into a fresh TC solution with PMS for TC catalytic degradation.

2.6. Construction of a monolith stirrer for catalysis and photothermal evaporation

2.6.1. Monolith stirrer for catalytic degradation. To assess the versatility of the catalyst in degrading pollutants, the catalyst was integrated into an immobilized recyclable sponge device for the catalytic degradation of pollutants in water. Briefly, 20 mg of catalyst was dispersed into a solution containing 14 mg of sodium alginate and 6 ml of water. An appropriate amount of the above-mentioned solution was dropped evenly in the circular sponge. Then the sponge containing the catalysts was transferred to a calcium chloride solution for cross-linking to anchor the catalysts. The above-mentioned process was repeated until all catalysts were completely cross-linked on the original sponge. The sponge devices were floated in a contaminant-containing solution with a 20 ppm solution of tetracycline and their degradation efficiency was assessed by UV spectrophotometry.

2.6.2. Evaluation of photothermal evaporation performance. The above-obtained monolith catalyst can be directly used as the photothermal test membrane. The beakers containing 50 ml of 20 ppm TC solution and a photothermal test membrane were placed under a solar simulator where the light intensity was maintained at 1 kW m^{-2} (one sun), as measured using an optical power meter (FZ400, NBeT, Beijing, China). The surface temperature of the film was measured every 60 s using an infrared camera, and the mass change of evaporated water was measured every 100 s using an electronic balance. The photothermal conversion efficiency and water evaporation rate of the catalyst were both obtained by data processing.

3. Results and discussion

3.1. Morphologic and structural analysis

Based on the concept of the above-mentioned strategy, as shown in Fig. 1(a), Ni-doped hydroxy-alumina composites were first prepared using dopamine (DA) as a modified agent. The *in situ* polymerization of DA incorporated cobalt ions in the polymer layer deposited on the AlOOH hydrangea. The subsequent thermal transformation process of the resulting composite was conducted in an N_2 atmosphere at different temperatures (400, 500, and 600 °C). The temperature-determined comparative sample characterization will be discussed in the later section. Through representative SEM images (Fig. 1(b)), it can be seen that the synthesized $Ni/Al_2O_3@Co_{500}$ catalyst presents a hydrangea-shaped morphology, consisting of a large number of corrugated nanosheets with an average diameter of 3–6 μm. However, the $Al_2O_3@Co_{500}$ catalyst without Ni doping was irregular and flaked, which formed a sharp contrast between the two shapes (Fig. S1†). Therefore, the hydrangea-shaped morphology of the $Ni/Al_2O_3@Co_{500}$ catalyst may be beneficial to improve the surface affinity of the catalyst for pollutants diffused toward the reaction sites. The TEM images (Fig. 1(c)) show that the metal particles are evenly distributed on the corrugated nanosheets. In addition, Fig. 1(d) shows the statistical size distribution of metal nanoparticles in the $Ni/Al_2O_3@Co_{500}$ sample, indicating that the average particle size of the $Ni/Al_2O_3@Co_{500}$ sample is about 23 nm. To further determine the existence status of metal species in the hydrangea-shaped $Ni/Al_2O_3@Co_{500}$, the elemental composition and distribution of the active substances were ascertained using a high-angle toroidal dark-field scanning transmission electron microscope (HAADF-STEM) and EDX mapping analysis. As shown in Fig. 1(e), $Ni/Al_2O_3@Co_{500}$ contains C, N, O, Co, Ni, and Al elements distributed on the surface of hydrangea-shaped $Ni/Al_2O_3@Co_{500}$. These observed elements show uniform distribution in the composite catalyst, indicating the efficient integration of Co, C, and N species by a polydopamine modification strategy. The dense distribution of Co and Ni on the support would ensure that the interaction of these two metals triggers possible electron transfer and improves the redox cycle. In the meantime, the presence of carbon and nitrogen on the surface of Al_2O_3 demonstrates the success of graphitization for the PDA layer. In addition, the existing N species in the carbon framework could improve the surface affinity of catalysts, which is beneficial to the accessibility of polar pollutants. This would make the generated ROS rapidly attack the adjacent pollutant molecule, which could shorten the diffusion distance of ROS and improve the utilization of ROS.

3.2. Surface property and crystalline state analysis

The phase crystal structures of $Ni/Al_2O_3@Co_{500}$ and $Al_2O_3@Co_{500}$ catalysts were studied by X-ray diffraction (XRD). As shown in Fig. 2(a and b), the dominant phase component of the $Ni/Al_2O_3@Co_{500}$ catalyst is consistent with metallic Ni (JCPDS No. 04-0850) or metallic Co (JCPDS No. 15-0806). In contrast, the main phase component of the $Al_2O_3@Co_{500}$ catalyst is mainly attributed to Al_2O_3 (JCPDS No. 37-1462). This combined result indicates that Ni and Co would be sintered into a superstructure of Ni–Co alloy from the initial composite.[21] The formation of Ni–Co alloy bonds may be attributed to that the carbon layer resulting from the PDA may prevent

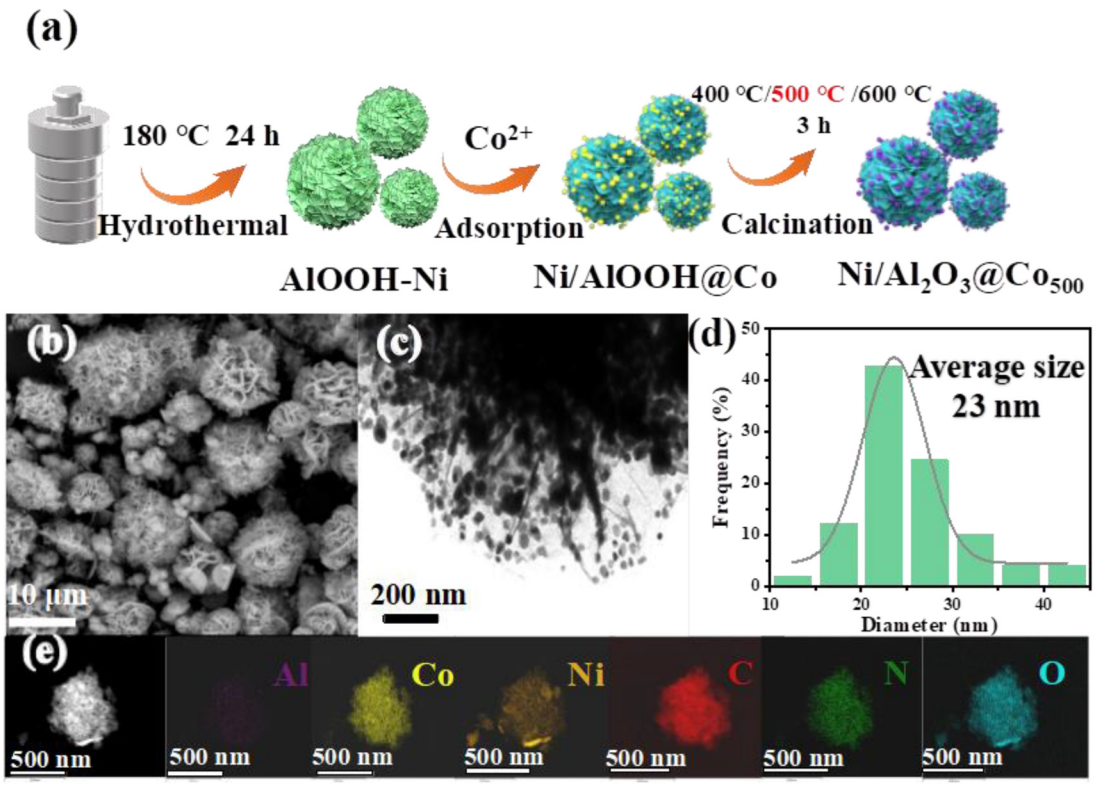

Fig. 1 (a) Schematic of the synthesis of $Ni/Al_2O_3@Co_{500}$ catalyst. (b) SEM image, (c) representative TEM image, (d) statistical graph of particle size distribution, and (e) TEM image of $Ni/Al_2O_3@Co_{500}$ and EDX mapping images of corresponding Al, Co, Ni, C, N, and O elements.

oxidation of the two metals onto a support and in favor of the alloying process of Co–Ni. The structure of catalysts and the existence of the carbon layer were further analyzed by Raman spectroscopy. As shown in Fig. 2(c), the peaks of the D band and G band of $Ni/Al_2O_3@Co_{600}$, $Ni/Al_2O_3@Co_{500}$, and $Ni/Al_2O_3@Co_{400}$ are generally located at 1350 and 1600 cm^{-1}, respectively, reflecting the degree of graphitization.[22] I_D/I_G is the intensity ratio of peak D to peak G, which is used to evaluate the quality, structure, and purity of the carbon material.[23] The highest I_D/I_G ratio among the three catalysts was 0.347 of $Ni/Al_2O_3@Co_{500}$. This high-carbon defect level indicated that the $Ni/Al_2O_3@Co_{500}$ catalyst possibly affords more surface polarity and optimizes the electronic structure of metal species.

To further analyze the surface elements, X-ray photoelectron spectroscopy (XPS) was performed. As shown in Fig. S2,† both $Ni/Al_2O_3@Co_{500}$ and $Al_2O_3@Co_{500}$ are composed of C, N, O, Co, and Al elements, and $Ni/Al_2O_3@Co_{500}$ contains additional Ni metal elements. The high-resolution spectrum of Al 2p of $Al_2O_3@Co_{500}$ shown in Fig. 2(d) presents two peaks at 73.4 and 74.3 eV corresponding to Al $2p_{1/2}$ and Al $2p_{3/2}$, respectively, while the peak position of Al 2p in $Ni/Al_2O_3@Co_{500}$ shows a slightly positive movement, and a Ni 3p cross peak at 67.35 eV associated with Ni(II) also obviously appears, indicating the electron transfer from Al to Ni *via* Ni–Al interaction in $Ni/Al_2O_3@Co_{500}$.[24] In addition, the Ni(0) core levels existed in $Ni/Al_2O_3@Co_{500}$. In parallel, as shown in Fig. 2(e), all the Co 2p spectra only presented two elemental states including Co(II) and Co(III) in the Co $2p_{1/2}$ and Co $2p_{3/2}$ core levels.[25] This result further indicates the dominant phase of metallic Ni in $Ni/Al_2O_3@Co_{500}$, while Co more possibly alloyed with the metallic Ni with more surface oxidation behavior for Co. The Co 2p spectrum of $Ni/Al_2O_3@Co_{500}$ is fitted into two main peaks of Co $2p_{3/2}$ and Co $2p_{1/2}$ located at 780.0 and 796.1 eV, respectively. Notably, $Ni/Al_2O_3@Co_{500}$ has a high Co(II) and Co(III) proportion due to its small size and high surface oxidation behavior, benefiting the PMS molecule activation in the catalytic reaction.[26–28] As shown in Table S1,† it can be clearly seen that the content of Co^{2+} species in $Ni/Al_2O_3@Co_{500}$ is 64.80% higher than that in $Al_2O_3@Co_{500}$ (54.93%). Co^{2+} species as mediators play an important role in electron transfer, promoting the activation of PMS and contributing to the generation of reactive oxygen species with a high redox potential, which is beneficial for the mineralization of organic pollutants. The XPS core level spectra of Ni 2p derived from $Ni/Al_2O_3@Co_{500}$ are shown in Fig. 2(f), split into Ni^{2+} and Ni^0 spectrum, as well as the acromion of metal $Ni^{\delta+}$. The peaks of the Ni^{2+} spectrum are situated at binding energies of 855.7 and 873.5 eV, respectively, and the satellite peaks are situated at binding energies of 861.5 and 880.0 eV,[29–32] respectively. The metal Ni^0 peak appears at about 852.4 eV, and the acromion of metal $Ni^{\delta+}$ appears at about 853.8 eV, indicating a strong Ni–Al interaction and Ni–Al bond in $Ni/Al_2O_3@Co_{500}$,[33,34] which may be related to the catalytic performance of $Ni/Al_2O_3@Co_{500}$.

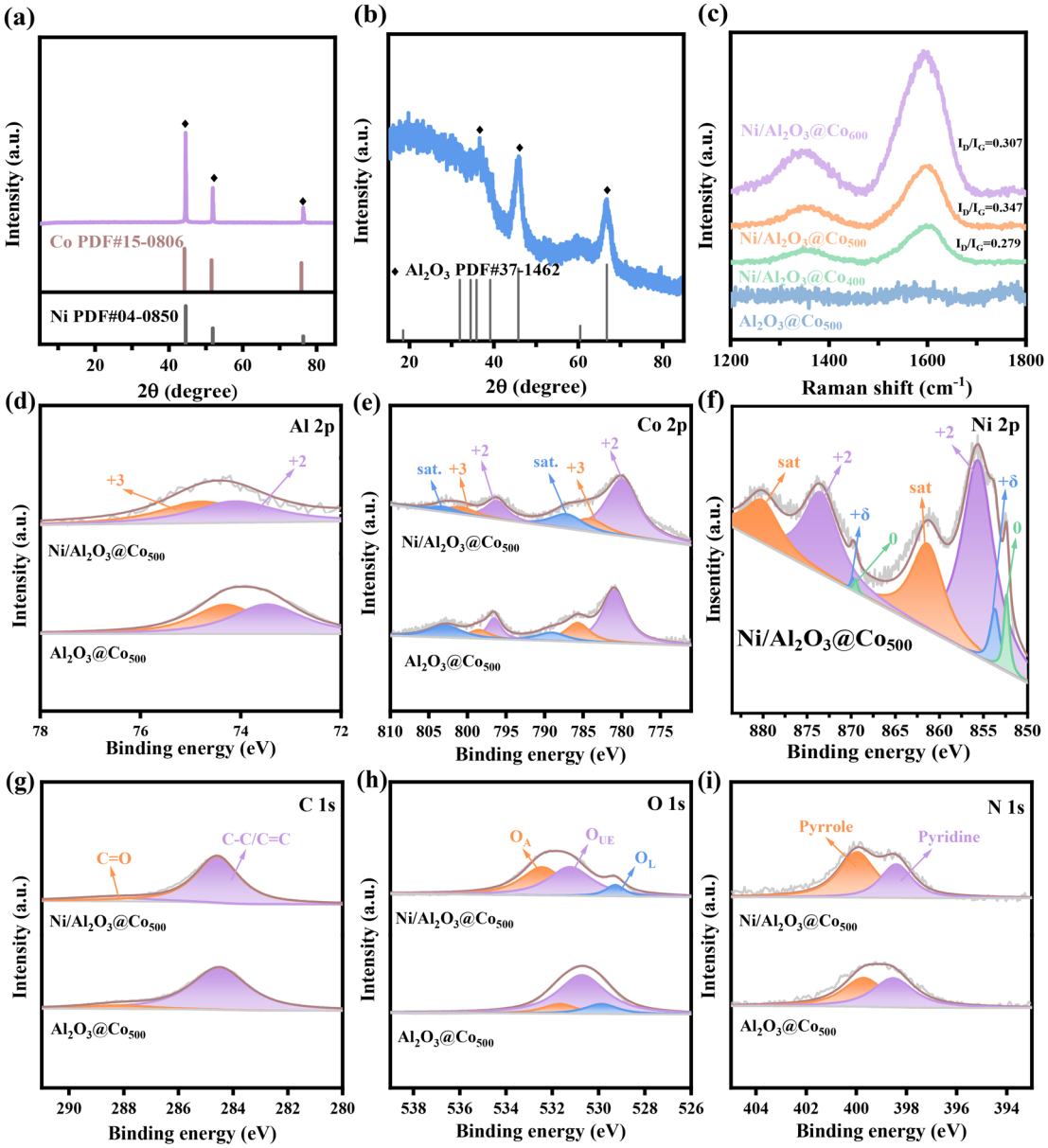

Fig. 2 Wide-angle XRD patterns of (a) Ni/AlOOH@Co_{500} and (b) AlOOH@Co_{500}. (c) Raman spectra of Ni/AlOOH@Co_{600}, Ni/AlOOH@Co_{500}, Ni/AlOOH@Co_{400} and AlOOH@Co_{500} composites. XPS core-level spectra of Al 2p (d), Co 2p (e), Ni 2p (f), C 1s (g), O 1s (h), and N 1s (i) derived from Ni/Al_2O_3@Co_{500} and Al_2O_3@Co_{500}.

As shown in Fig. 2(g), the high-resolution C 1s spectra of the two catalysts can be deconvolved into two peaks including Sp^2-hybrid carbon (284.6 eV) and C═O (288.6 eV), indicating that there are abundant carbon species on the surface of the carbon, beneficial to improve the surface affinity of the catalyst to capture polar pollutants around the reaction sites.[35] The O 1s spectrum of Ni/Al_2O_3@Co_{500} was split into lattice oxygen (O_L), unpaired electron oxygen (O_{UE}), and surface-adsorbed oxygen (O_A) at binding energies of 529.25, 531.20, and 532.30 eV, respectively (Fig. 2(h)). As shown in Table S1,† the proportion of O_A in Ni/Al_2O_3@Co_{500} is much higher than that in Al_2O_3@Co_{500}, contributing to reducing the activation energy of the reaction and increasing the reaction rate. This higher oxygen content is also attributed to the ability of surface oxygen as an acidic intermediate to enhance the catalytic reaction.[36] Fig. 2(i) shows the high-resolution N 1s spectral partitioning of all catalysts as pyridine N (398.3 eV) and pyrrole N (400.0 eV).[37] As shown in Table S1,† the proportion of pyrrole nitrogen in Ni/Al_2O_3@Co_{500} is higher than that of pyridine nitrogen, indicating the high intrinsic catalytic performance of pyrrole nitrogen, while the proportion of pyrrole N and pyridine N in the Al_2O_3@Co_{500} sample is subequal. The activity of pyrrole N will be inhibited due to the interaction with the nearby pyridine N sites,[38] and hence, the catalytic effect of Al_2O_3@Co_{500} may be inferior to that of Ni/Al_2O_3@Co_{500}.

3.3. Electrochemical analysis

To study the electrochemical characteristics of Ni/Al_2O_3@Co_{500} and Al_2O_3@Co_{500}, we performed electrochemical impedance spectroscopy, linear scanning voltammetry, electrochemical double-layer capacitors, cyclic voltammetry, and open circuit voltage measurements (Fig. 3). As shown in Fig. 3(a), the diameter of the arc shape of Ni/Al_2O_3@Co_{500} is smaller than that of Al_2O_3@Co_{500}, indicating that Ni/Al_2O_3@Co_{500} has extremely low charge transfer resistance and the efficient charge transfer. The linear sweep voltammetry (LSV) measurement in Fig. 3(b) was to study the electrochemical activity of the electrode materials of the two catalysts. The corrosion potential of the two catalysts is both negative, while the corrosion potential of Ni/Al_2O_3@Co_{500} (−0.303 eV) is smaller than that of Al_2O_3@Co_{500} (−0.292 eV). This phenomenon indicates that Ni/Al_2O_3@Co_{500} has an obvious electron transfer advantage and can start a redox reaction at a lower potential, in accordance with the EIS results, in favor of the superior catalytic performance on the degradation of pollutants. Moreover, the smaller corrosion potential may mean that the electrode reaction of the material is more active, which can not only provide a higher current density and good electrochemical performance but also improve the electrocatalytic efficiency and optimize the electrochemical process. The electrochemical surface area (ECSA) was determined by the double-layer capacitance (C_{dl}) shown in Fig. 3(c). Compared with the ECSA of Al_2O_3@Co_{500} (0.19 mF cm^{-2}), Ni/Al_2O_3@Co_{500} (0.30 mF cm^{-2}) shows a higher ECSA, indicating the presence of more active sites in Ni/Al_2O_3@Co_{500}, which may be conducive to activating PMS to degrade TC. To further study the redox behavior of electrochemically active substances, cyclic voltammetry (CV) is used to measure the change in current with voltage through repeated scanning within a certain voltage range shown in Fig. 3(d and e). The ring of Ni/Al_2O_3@Co_{500} is larger than that of Al_2O_3@Co_{500}, which means that the current density of Ni/Al_2O_3@Co_{500} increases quickly and the overpotential (η) changes little. This indicated that Ni/Al_2O_3@Co_{500} has higher efficiency and stability in the catalytic reaction. To further study the reasons for the superior catalytic performance, we tested the open circuit voltage. As shown in Fig. 3(f), when only TC is added, the input voltage changed little compared with Al_2O_3@Co_{500}, indicating that there was no obvious electron transfer when Ni/Al_2O_3@Co_{500} was alone, so Ni/Al_2O_3@Co_{500} shows a stronger adsorption effect on the pollutant. Thus, the enrichment of pollutants on the catalyst surface is promoted, the contact area of the reaction is increased, and the reaction efficiency is improved.

3.4. Catalytic performance analysis

To evaluate the catalytic performance of Ni/Al_2O_3@Co_{400}, Ni/Al_2O_3@Co_{500}, Ni/Al_2O_3@Co_{600}, Al_2O_3@Co_{500}, and Ni/Al_2O_{3-500}

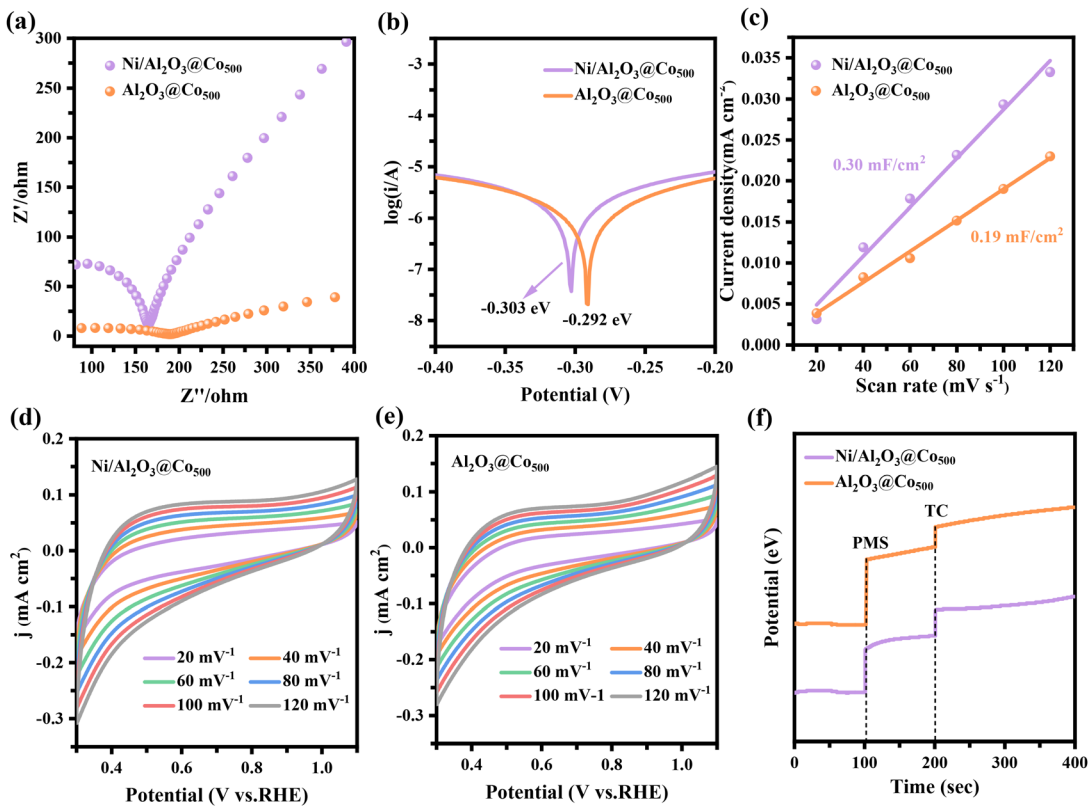

Fig. 3 (a) Electrochemical impedance spectra (EIS), (b) linear scanning voltammetric (LSV) curves, and (c) electrochemical double-layer capacitors of Ni/Al_2O_3@Co_{500} and Al_2O_3@Co_{500}. Cyclic voltammetric curves of (d) Ni/Al_2O_3@Co_{500} and (e) Al_2O_3@Co_{500} at different scan rates (20–120 mV s^{-1}) in the range of 0.3–1.1 V relative to RHE. (f) Open circuit voltage test for Ni/Al_2O_3@Co_{500} and Al_2O_3@Co_{500}.

catalysts, the degradation of 20 mg L^{-1} of TC solution with the reaction of oxidant PMS was tested using a UV spectrophotometer, and pre-adsorption experiments were also carried out. Fig. 4 shows the degradation kinetic curves and three-dimensional fluorescence spectra of the catalysts. As shown in Fig. 4(a), under the same condition, the catalyst calcined at 500 °C ($Ni/Al_2O_3@Co_{500}$) had the fastest catalytic reaction rate during the degradation process among the catalysts, and the reactivity of the catalysts calcined at different temperatures is in the order of $Ni/Al_2O_3@Co_{500}$ > $Ni/Al_2O_3@Co_{600}$ > $Ni/Al_2O_3@Co_{400}$. It was attributed to the higher calcination temperature that resulted in the growth of AlOOH aggregates, leading to a reduction in the active sites of the catalyst. Lower calcination temperatures cannot allow for sufficient trimetallic synergism to form in the alloys of Al, Ni, and Co, due to the higher surface oxidation behavior of the alloys at smaller sizes.[39] The fitted values of the slope of the reaction rate constants (k) in Fig. 4(b) prove that $Ni/Al_2O_3@Co_{500}$ (0.498 min^{-1}) calcined at a temperature of 500 °C is optimal, while the k values of $Ni/Al_2O_3@Co_{400}$ and $Ni/Al_2O_3@Co_{600}$ are 0.120 and 0.217 min^{-1}, respectively. For the two catalysts prepared at the same temperature with different precursors, the catalytic activity of $Ni/Al_2O_3@Co_{500}$ is superior to that of $Al_2O_3@Co_{500}$ and Ni/Al_2O_{3-500} (Fig. 4(a)), which may be attributed to the combination of the added Ni with Al and Co to form sufficient Ni–Al–Co trimetallic synergy. The reaction rate constants in Fig. 4(b) demonstrate that the catalytic activity of $Ni/Al_2O_3@Co_{500}$ (0.498 min^{-1}) is superior to that of $Al_2O_3@Co_{500}$ (0.362 min^{-1}) and Ni/Al_2O_{3-500} (0.065 min^{-1}).

Three-dimensional fluorescence spectroscopy is used to study intermediate products and mineralization levels during degradation.[40] The degradation pathway of the antibiotic TC is not completely separated and its intermediate products may be interconverted in the reaction process. In addition, TC will produce obvious fluorescence signals during the degradation process by three-dimensional fluorescence spectroscopy. At 0 min, no $Ni/Al_2O_3@Co_{500}$ catalyst was added to the TC and the reaction did not start, so no intermediates were produced, as shown in Fig. 4(c). At a reaction time of 1 min, Fig. 4(d) shows distinct characteristic loops between 350 and 500 nm, which can be attributed to the fulvic acid-associated fluorescence region.[41] After reacting for 10 min, a significant increase in the characteristic loop can be observed in Fig. 4(e), and at 20 min, there was a gradual decrease in the characteristic loop in the range of 350–450 nm, as shown in Fig. 4(f). The fluorescence intensity showed a trend of first increasing and then decreasing, indicating that TC was first degraded into fulvic acid organic matter during the reaction,[42] and then further mineralized into intermediates with a reduced molecular weight.

To find out the optimal reaction conditions that would enable the optimal $Ni/Al_2O_3@Co_{500}$ catalyst to perform the best degradation performance, the condition experiments to find the optimal catalyst dosage, PMS dosage, TC concentration, and reaction temperature were surveyed. As shown in Fig. 5(a and d), the rate of catalytic degradation of TC was positively correlated with the $Ni/Al_2O_3@Co_{500}$ concentration. When the catalyst concentration increases from 0.2 to 0.6 g L^{-1}, the reaction constant also increases. While compared with that of 0.4 g L^{-1}, the degradation constant at a $Ni/Al_2O_3@Co_{500}$ concentration of 0.6 g L^{-1} was not significantly improved, indicating that 0.4 g L^{-1} catalyst was sufficient to degrade TC. As

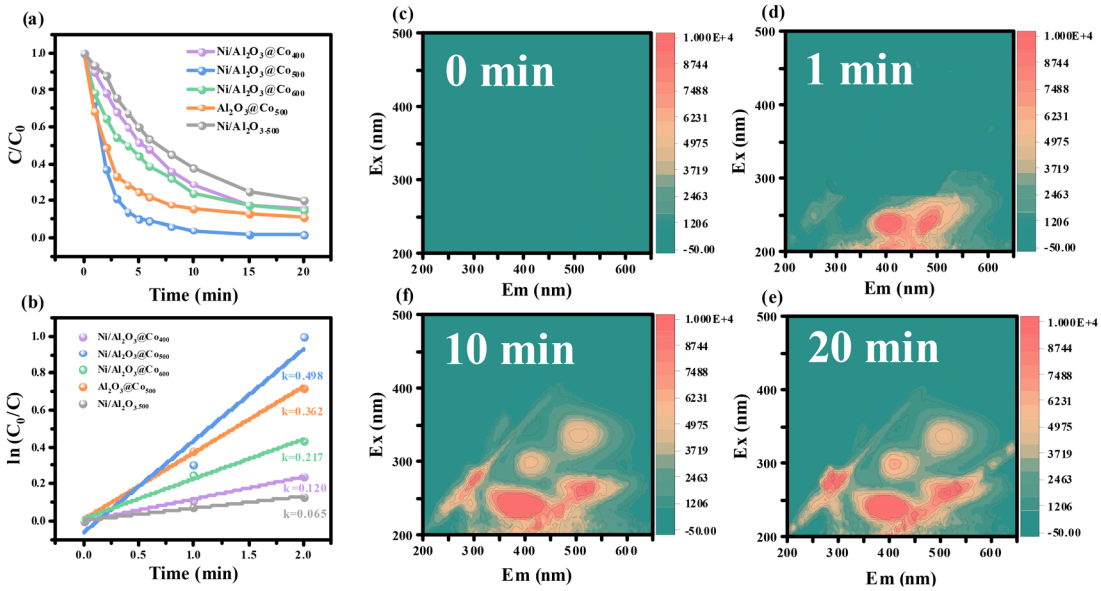

Fig. 4 Time-dependent catalytic degradation course curves of TC on $Ni/Al_2O_3@Co_{400}$, $Ni/Al_2O_3@Co_{500}$, $Ni/Al_2O_3@Co_{600}$, $Al_2O_3@Co_{500}$ and Ni/Al_2O_{3-500} samples: (a) relationship between C/C_0 and reaction time, and (b) reaction rate. Reaction conditions: [TC] = 20 mg L^{-1}, [PMS] = 0.4 g L^{-1}, and [catalyst] = 0.4 g L^{-1}. Three-dimensional fluorescence spectra of $Ni/Al_2O_3@Co_{500}$ in the process of catalytic degradation of TC at the reaction time of (c) 0, (d) 1, (e) 10, and (f) 20 min. Reaction condition: [TC] = 20 mg L^{-1}, [PMS] = 0.4 g L^{-1}, [catalyst] = 0.4 g L^{-1}, and temperature = 25 °C.

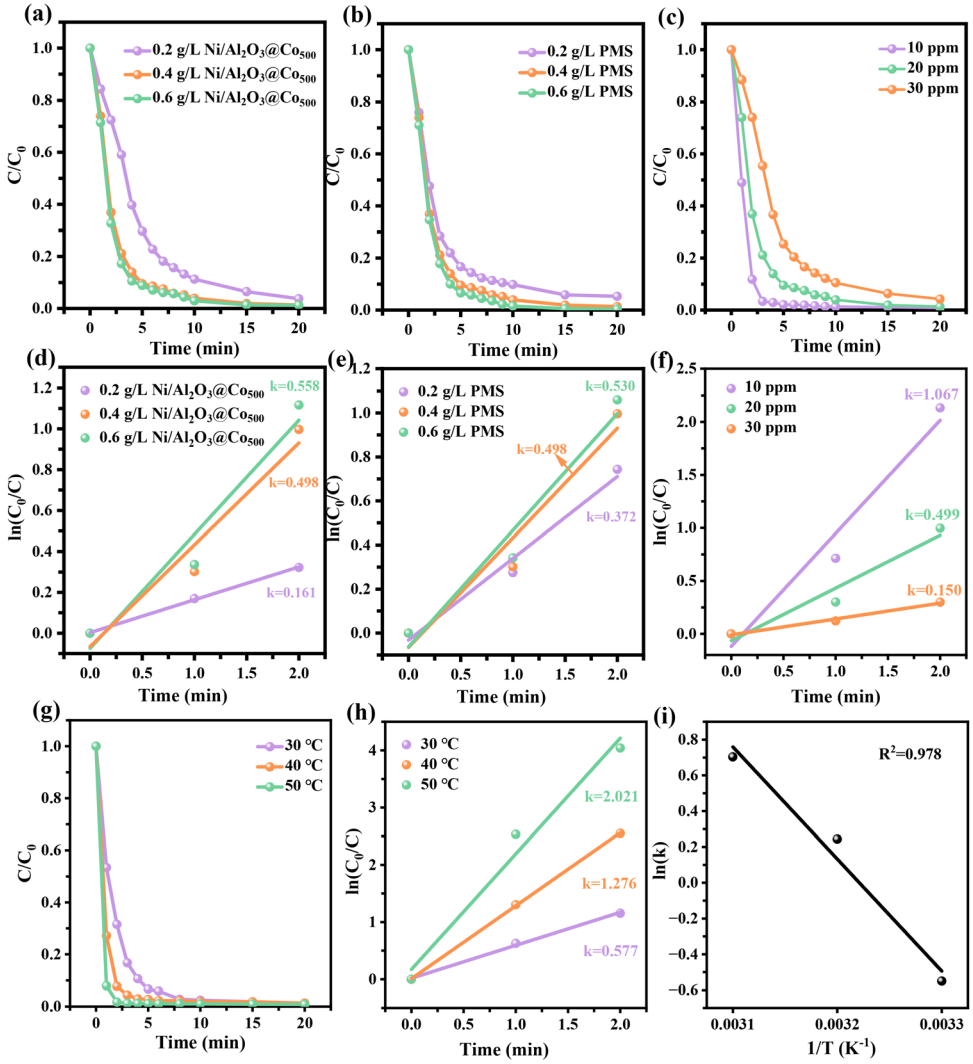

Fig. 5 (a) Time-dependent TC degradation course curves over $Ni/Al_2O_3@Co_{500}$ using different catalyst dosages and (d) corresponding kinetic curves of $\ln(C_0/C)$ *vs.* reaction time. Reaction condition: [TC] = 20 mg L^{-1}, [PMS] = 0.4 g L^{-1}, and temperature = 25 °C. (b) Time-dependent TC degradation course curves over $Ni/Al_2O_3@Co_{500}$ using different PMS dosages, and (e) corresponding kinetic curves of $\ln(C_0/C)$ *vs.* reaction time. Reaction condition: [TC] = 20 mg L^{-1}, [catalyst] = 0.4 g L^{-1}, and temperature = 25 °C. (c) Time-dependent TC degradation course curves over $Ni/Al_2O_3@Co_{500}$ using different TC concentrations, and (f) corresponding kinetic curve of $\ln(C_0/C)$ *vs.* reaction time. Reaction condition: [catalyst] = 0.4 g L^{-1}, and [PMS] = 0.4 g L^{-1}, and temperature = 25 °C. (g) Time-dependent TC degradation course curves over $Ni/Al_2O_3@Co_{500}$ at different reaction temperatures, and (h) corresponding kinetic curves of $\ln(C_0/C)$ *vs.* reaction time. Reaction condition: [TC] = 20 mg L^{-1}, [PMS] = 0.4 g L^{-1}, and [catalyst] = 0.4 g L^{-1}. (i) Corresponding kinetic curves of $\ln(k)$ *vs.* T^{-1}.

shown in Fig. 5(b) and (e), the reaction rate of catalysis also increased when the PMS concentration was increased from 0.2 to 0.4 g L^{-1}, which can be explained by the fact that more free radicals were generated with the increase in the PMS concentration to promote the degradation of the pollutants in the water column.[43] When the PMS content was increased to 0.6 g L^{-1}, the reaction constant was not significantly improved, indicating that the free radicals generated by 0.4 g L^{-1} PMS were sufficient to promote the degradation of pollutants. Then, we also adjusted the concentration of the pollutant TC solution (shown in Fig. 5(c) and (f)). At a TC solution concentration of 10 mg L^{-1}, $Ni/Al_2O_3@Co_{500}$ degraded the pollutant completely within 5 min, with a reaction rate constant of 1.067 min^{-1}. In addition, when the TC concentration was up to 20 and 30 mg L^{-1}, the reaction rate constant declined. The temperature during the reaction is also an important factor affecting the degradation of pollutants by the catalyst. Fig. 5(g) shows the degradation response of $Ni/Al_2O_3@Co_{500}$ to TC at different temperatures as a function of time. The results showed that the rate of TC degradation increased gradually with the increase in temperature. When the temperature reached 50 °C, the degradation process could be completed within 2 min. Fig. 5(h) shows the kinetic curves obtained by linear fitting of the reaction rate constants at different temperatures, which proved that the temperature was positively correlated with the catalytic efficiency, and the order of the reaction activity at

different temperatures was 50 °C (2.021 min^{-1}) > 40 °C (1.276 min^{-1}) > 30 °C (0.577 min^{-1}). Using the Arrhenius equation,[44] the activation energy of Ni/Al_2O_3@Co_{500} was calculated as 52 kJ mol^{-1}. The formula for the calculation of reaction activation energy (E_a) is $\ln k = -E_a/RT + \ln A$, where A is the Arrhenius constant, E_a represents the activation energy (kJ mol^{-1}), T is the absolute temperature (K), and R is the gas constant (J mol^{-1} K^{-1}). From the slope of the line, the value of R^2 was calculated to be 0.978 (Fig. 5(i)). To fully summarize the benefits of synthesized Ni/Al_2O_3@Co_{500}, we compared the Ni/Al_2O_3@Co_{500}/PMS system with other reported catalyst systems, including contaminant concentration, catalyst concentration, PMS concentration, reaction temperature, degradation time, reaction rate constant, and degradation efficiency (listed in Table S2†). The catalytic degradation performance of Ni/Al_2O_3@Co_{500} is comparable. Thus, Ni/Al_2O_3@Co_{500} can realize rapid mineralization of pollutants and show high catalytic degradation performance.

3.5. Catalytic mechanism and interferences

To further study the influence of various active substances on the catalytic degradation reaction, different quenchers were selected for radical quenching. Methanol (MeOH) and *tert*-butanol (TBA) were used to quench hydroxyl radicals ($OH^•$) and sulfate radical anions ($^•SO_4^-$),[45,46] respectively. Since MeOH acts on $^•SO_4^-$ and $OH^•$, and TBA only acts on $OH^•$, TBA and MeOH can be used to distinguish the effects of $^•SO_4^-$ and $OH^•$ on the reaction. L-Histidine (L-his) and *p*-benzoquinone (P-BQ) were used to quench singlet oxygen ($^1O_2$) and superoxide free radicals ($^•O_2^-$) to determine the degree of their influence on the reaction.[47] As shown in Fig. 6(a) and (d, g), the calculated quenching rate constants of P-BQ, L-his, TBA, and MeOH were 0.094, 0.148, 0.101, and 0.073 min^{-1}, respectively, so the rate constant of the reaction is significantly reduced by the presence of free radical quencher compared with that of the original reaction (0.494 min^{-1}). According to the calculation, the proportion of P-BQ, L-his, TBA, and MeOH quenching on the catalytic TC degradation reaction is 81.0%, 70.0%, 79.6% and 85.2%, respectively. Therefore, by calculating the contributions of different radicals, O_2^- is the main active substance (about 81.0%), $^•OH$ (79.6%) and $^1O_2$ (70.0%) play important roles in the radical pathway, and SO_4^- (5.6%) contributes to the least activity during the TC degradation. Thus, various active substances play an important role in the degradation of TC and may have synergistic effects on TC degradation.

In practical applications, the presence of certain anions can also affect the catalytic performance. Fig. 6(b) shows the time change curve of the degradation reaction with the addition of catalysts and different anions in 20 mg L^{-1} TC solution. The results shown in Fig. 6(e) and (h) revealed that the order of anions inhibiting TC degradation was OH^- > HCO_3^- > CO_3^{2-} > Cl^- > SO_4^{2-}, and SO_4^{2-} can facilitate the TC degradation in the Ni/Al_2O_3@Co_{500}/PMS system. Compared with other anions, SO_4^{2-} has less inhibitory effects on degradation, because SO_4^{2-} has a strong oxidation effect and can interact with the molecular structure of organic matter to achieve the purpose of TC degradation.[48] The strong inhibitory effect of OH^- on TC degradation may be related to the change of pH in the reaction solution caused by its hydrolysis,[49] which indicates that the base anions may be unfavorable to the removal of TC in water with Ni/AlOOH@Co_{500}.

To verify the feasibility of Ni/Al_2O_3@Co_{500}, we further studied the catalytic degradation of methylene blue (MB), norfloxacin (NFX), bisphenol A (BPA), and oxytetramycin (OTC). Fig. 6(c) shows the curve of catalytic degradation of different pollutants by Ni/Al_2O_3@Co_{500} over the reaction time. Ni/Al_2O_3@Co_{500} not only has a good degradation effect on TC but also has a removal rate of MB up to 100% within 7 min. Under the same conditions, it also has a degradation effect on other pollutants. Fig. 6(f) and (i) reveal that the order of the efficacy of pollutant degradation within 2 min was TC > OTC > MB > BPA > NFX. In addition to the degradation of individual organic pollutants, the removal of multiple pollutants is critical, and hence, pollutant degradation was assessed using total organic carbon (TOC) changes. We investigated the mineralization ability of the Ni/Al_2O_3@Co_{500}/PMS systems to several single contaminants including TC, BPA, NFX and their mixtures. After the addition of 0.4 g·L^{-1} Ni/Al_2O_3@Co_{500} and 0.4 g L^{-1} PMS, TOC removal rates for single-contaminant TC, BPA and NFX reached 30.8%, 41.7% and 10.7% (Fig. S3†) at a reaction time of 60 min, respectively. For two or more pollutants mixed in the Ni/Al_2O_3@Co_{500}/PMS system, TOC still has a certain removal effect, which is slightly weaker than that of a single pollutant. The results indicate that the Ni/Al_2O_3@Co_{500}/PMS system has satisfactory mineralization capacity and may be suitable for treating practical wastewater treatment applications.

3.6. Practical application of catalysts

Considering the practical application feasibility of Ni/Al_2O_3@Co_{500}, we explored the catalysis performance of Ni/Al_2O_3@Co_{500} in different actual water sources. The water sources from Haiyun Lake situated in Zhenjiang City Jiangsu Province China and ordinary tap water are used as solvents to prepare a TC solution with a concentration of 20 mg L^{-1} for the degradation experiment. As shown in Fig. S4(a) and Fig. S4(b),† the degradation effect of the solution mixed with tap water and lake water was lower than that of deionized water, which may be attributed to Cl^- in tap water, inhibiting the reaction. Although the lake water has been filtered to remove impurities, there are still many residual substances affecting the catalysis degradation. However, all the degradation rates of Ni/Al_2O_3@Co_{500} in three actual water sources are still maintained up to 90%. Overall, the actual water source has little effects on the catalytic performance of Ni/Al_2O_3@Co_{500}, which may be due to the stability of the synergistic interaction between the three metals, further highlighting the advantages of the catalyst.

Research on the reusability of Ni/Al_2O_3@Co_{500} is also conducted. In each cycle of the reaction, Ni/Al_2O_3@Co_{500} was obtained and heated in an N_2 atmosphere at 300 °C for acti-

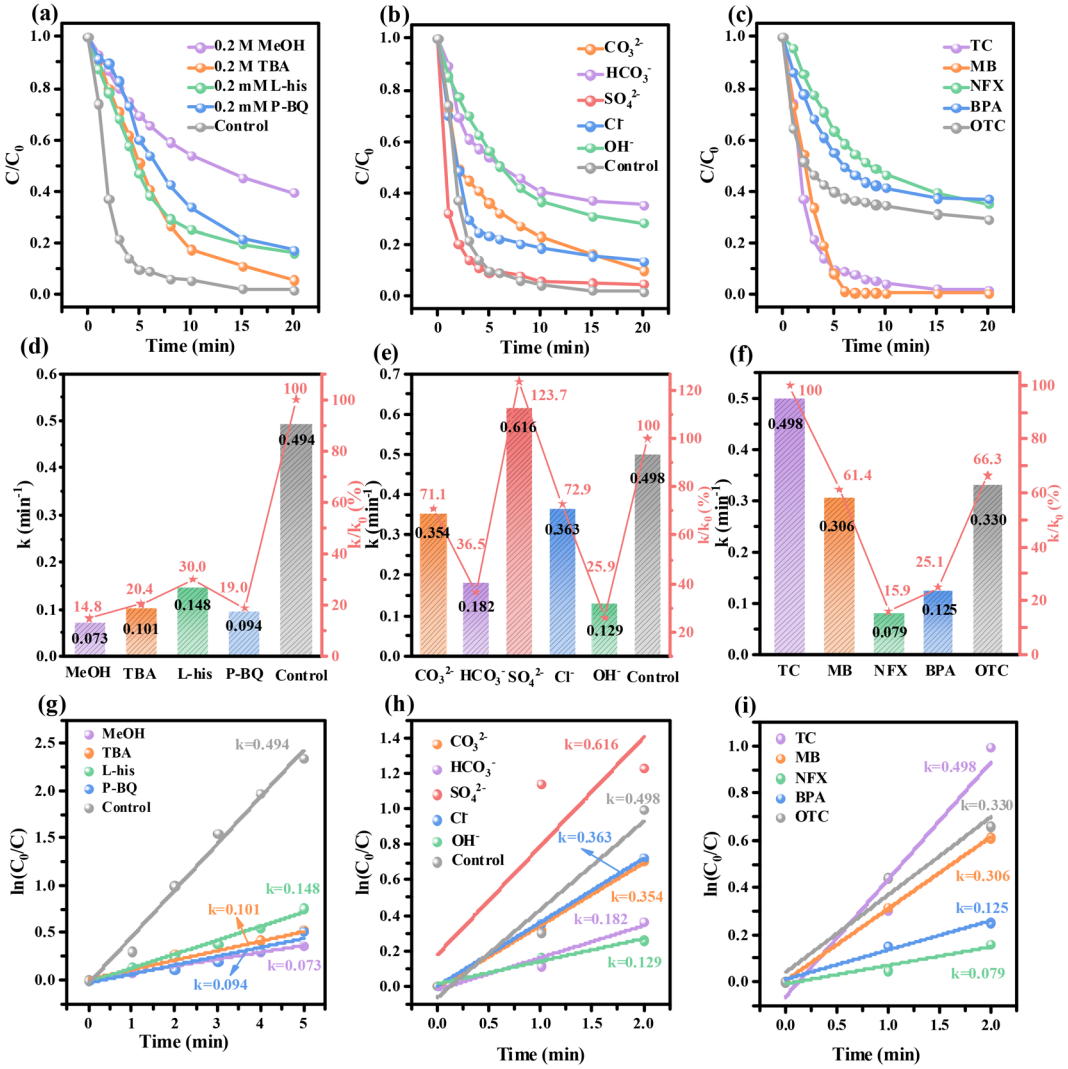

Fig. 6 (a) Effect of quenching agents of P-BQ, L-his, TBA, or MeOH on TC degradation in the Ni/Al_2O_3@Co_{500}/PMS system and (d) histogram of the corresponding calculated reaction rate constants. Reaction condition: [MeOH] = 0.2 mol L^{-1}, [TBA] = 0.2 mol L^{-1}, [P-BQ] = 0.2 mmol L^{-1}, [L-his] = 0.2 mmol L^{-1}. (b) Time-dependent TC degradation course curves over Ni/Al_2O_3@Co_{500} with different anionic interferents and (e) histogram of the corresponding calculated reaction rate constants. Reaction condition: [TC] = 20 mg L^{-1}, [PMS] = 0.4 g L^{-1}, [catalyst] = 0.4 g L^{-1}, [anion] = 0.4 mol L^{-1}, Temperature = 25 °C. (c) Time-dependent pollutant degradation course curves over Ni/Al_2O_3@Co_{500} with different pollutant interferents and (f) histogram of the corresponding calculated reaction rate constants. Reaction condition: [Pollutants] = 20 mg L^{-1}, [PMS] = 0.4 g L^{-1}, [catalyst] = 0.4 g L^{-1}, Temperature = 25 °C. Linear graph of ln(C_0/C) with reaction time. (g) Kinetic reaction of the effects of quenching agents P-BQ, L-his, TBA or MeOH on TC degradation in the Ni/AlOOH@Co_{500}/PMS system; (h) kinetic reaction of TC degradation curve with time on Ni/AlOOH@Co_{500} with interference of different anions; and (i) Ni/AlOOH@Co_{500} kinetic reaction of pollutant degradation process with time under different pollutant interferences.

vation for 1 h. After three cycles, the degradation efficiency of Ni/Al_2O_3@Co_{500} decreased slightly (Fig. S5†), which may be due to the destruction of Ni–Al–Co alloy bonds by multiple calcination, resulting in the loss of catalyst mass, thus affecting the degradation efficiency of the reaction. Considering the actual application scenario that the powdered catalyst dispersed in contaminants is difficult to recover, Ni/Al_2O_3@Co catalysts are further cross-linked on the sponge by a calcium-triggered hydrogel-coating strategy. Fig. 7(a) presents a simple stirring propeller device for cross-linking integral catalysts, which can make the pollutants fully contact with the catalyst to improve the removal rate. Fig. 7(b–e) shows the cross-linked catalysts calcined at different temperatures on the differently shaped sponge sheets. The curves of TC degradation with reaction time in Fig. 7(f) show that the reaction rates and efficiency of the integrated catalyst synthesized by Ni/Al_2O_3@Co_{500} are superior to those synthesized by Ni/Al_2O_3@Co_{400} and Ni/Al_2O_3@Co_{600}, respectively, further confirming that Ni/Al_2O_3@Co_{500} is the optimal catalyst for TC degradation.

To further study the application of monolithic catalysts, we cut different polygonal and circular sponges for comparative

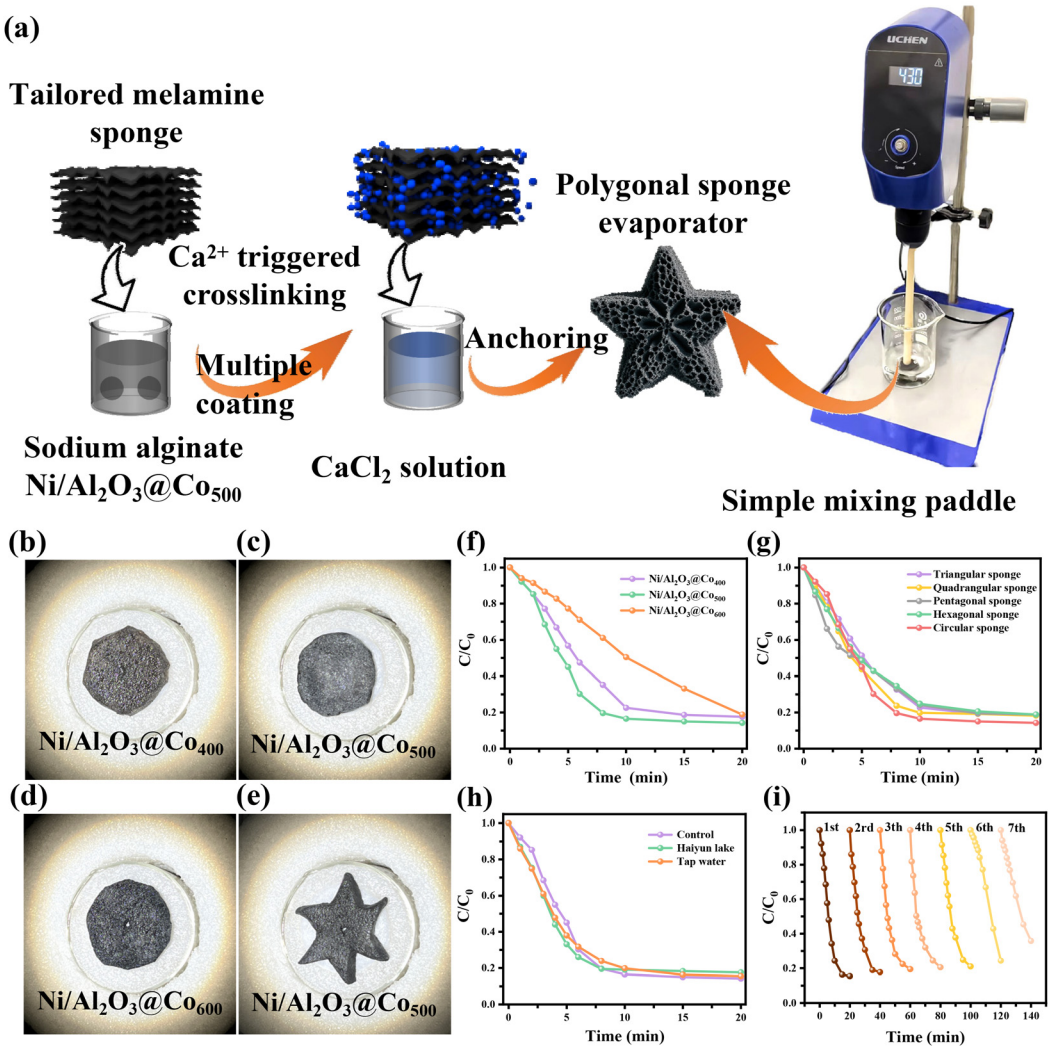

Fig. 7 (a) Polygonal sponge evaporator device manufacturing process and schematic of the actual catalytic test of the simple stirring paddle device for monolithic catalysts. Surface morphologies of different shaped sponge disks anchored by (b) $Ni/Al_2O_3@Co_{400}$, (c and e) $Ni/Al_2O_3@Co_{500}$, and (d) $Ni/Al_2O_3@Co_{600}$. (f) Kinetic curves of TC degradation by the integral catalyst of $Ni/Al_2O_3@Co_{400}$, $Ni/Al_2O_3@Co_{500}$, and $Ni/Al_2O_3@Co_{600}$. (g) Catalytic degradation of TC with time in a simple stirring apparatus for different shaped monolithic samples anchored by $Ni/Al_2O_3@Co_{500}$. (h) TC degradation curves of integrated catalyst $Ni/Al_2O_3@Co_{500}$ with reaction time in different actual water sources. (i) Integrated $Ni/Al_2O_3@Co_{500}$ catalyst for seventh consecutive TC degradation cycles.

experiments to study whether different shapes of sponges will have an impact on the experiment. As can be seen from Fig. 7(g), the shape of the carrier material had no significant effect on the degradation reaction, indicating that as long as the catalyst can be uniformly cross-linked on the sponge, the degradation effect of the integral catalyst can be normally played. To further explore the practical applications of the integrated catalyst $Ni/Al_2O_3@Co_{500}$, its performance was tested in different actual water sources, following the same procedure as that of the powder catalyst. Moreover, the TC solution with a concentration of 20 mg L^{-1} was prepared by using the water source of Haiyun Lake in Zhenjiang City, Jiangsu Province, and ordinary tap water as the solvent for the degradation experiment. It can be observed from Fig. 7(h) that the degradation performance of the solution made from tap water and lake water is slightly lower than that of the solution made from deionized water, possibly because Cl^- in tap water and the residual impurities in lake water affect the catalytic performance. In the two actual water sources, the degradation rate of integrated catalyst $Ni/Al_2O_3@Co_{500}$ remained above 80%. The reusability of the integrated catalyst $Ni/Al_2O_3@Co_{500}$ was also studied. As shown in Fig. 7(i), 65% degradation efficiency is still retained after 7 cycles. It can be seen that the integrated catalyst $Ni/Al_2O_3@Co_{500}$ has excellent recyclability and reusability. Compared with powder catalysts, the integrated catalyst has more advantages in the recovery method.

The powdered catalysts cross-linked on the sponge can be recycled, but some suspended and metal particles will still dissolve in the solution, posing a threat to human health. Therefore, the regeneration of clean water is crucial for us. To

further obtain clean water without pollution, we conducted a water evaporation experiment under the simulated solar illumination. The preparation process of the integral evaporator consisting of a melamine sponge and a photothermal catalyst according to related references[50–54] is shown in Fig. 7(a). The resulting sample is uniformly dispersed into the sodium alginate solution, and then the customized sponge is immersed in the mixture to further cross-link through the polymerization of the hydrogel network induced by Ca ions. The resulting integral evaporator can be cleverly placed in the polluted wastewater as a floating device, and the integral evaporator can also be combined with the stirring propeller to form a simple stirring paddle device. With the introduction of PMS, the system can be powered by solar energy, efficiently achieving water evaporation and simultaneous degradation of pollutants. Fig. S6(a–c)† presents the infrared thermograms reflecting the temperature variation in the process of water evaporation recorded using an infrared camera every 10 minutes. It can be found that the temperature of the Ni/Al_2O_3@Co_{500} coated film reaches up to 40.8 °C within 30 min, while the highest temperatures of NiAl_2O_3@Co_{400} and Ni/Al_2O_3@Co_{600} wet films are 38.8 °C and 40.3 °C, respectively. By comparison, it can be found that Ni/Al_2O_3@Co_{500} has slightly better photothermal conversion performance. Fig. 8(a and b) show the infrared thermal images acquired using an infrared camera, reflecting the temperature change in the process of integrated optimal catalyst promoting water evaporation. Fig. 8(c) shows the temperature variations of Ni/Al_2O_3@Co_{400}, Ni/Al_2O_3@Co_{500}, and Ni/Al_2O_3@Co_{600}-coated wet films in the evaporation process of water, presenting that the highest temperature of the Ni/Al_2O_3@Co_{500}-coated film can reach 41.4 °C with the irradiation time. As shown in Fig. 8(d), under the light irradiation, the evaporation rate of the wet film anchored by Ni/Al_2O_3@Co_{500} is 1.944 kg m^{-2} h^{-1}, and that of wet films anchored by Ni/Al_2O_3@Co_{400} and Ni/Al_2O_3@Co_{600} is 1.385 kg m^{-2} h^{-1} and 1.597 kg m^{-2} h^{-1}, respectively. The higher evaporation rate of Ni/Al_2O_3@Co_{500} may be attributed to the folds in the hydrangea-shaped structure of Ni/Al_2O_3@Co_{500} that provides more diffusion areas for the diffusion of water molecules from the film to the outer surface. Comparing the evaporation property of the catalyst system with others (Table S3†), it is clearly observed that Ni/Al_2O_3@Co_{500} has superior evaporation rate under sunlight, meaning that Ni/Al_2O_3@Co_{500} has great potential in solar water evaporation and water regeneration applications. Fig. S6(b, d)† and Fig. 8(e) reflect the temperature changes of circular and hexagonal wet films anchored by Ni/Al_2O_3@Co_{500} over irradiation time. As shown in Fig. 8(e), the circular wet film can heat up to 41.4 °C, while the highest temperature of the hexagonal wet film is 38.2 °C. Moreover, the evaporation rate shown in Fig. 8(f) of the circular wet film is 1.944 kg m^{-2} h^{-1} and that of the hexagonal wet film is 1.398 kg m^{-2} h^{-1}, and the photothermal conversion efficiency is 98.81%. Therefore, the circular wet film has better photothermal conversion performance, indicating that the shape of the sponge affects the photothermal conversion performance of the catalyst.

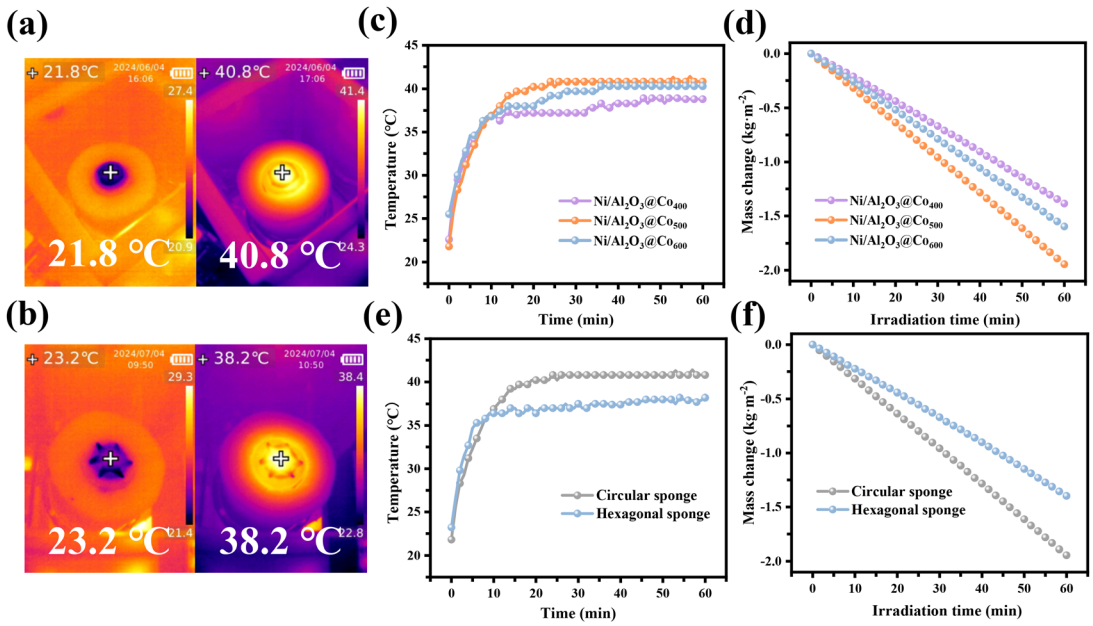

Fig. 8 Infrared thermogram of the temperature changes of the round wet film anchored by (a) Ni/Al_2O_3@Co_{500} and infrared thermogram of the temperature change of the polygonal wet film composed of (b) Ni/Al_2O_3@Co_{500} under sunlight irradiation. Variation in (c) surface temperature and (d) water mass of wet films anchored by Ni/Al_2O_3@Co_{400}, Ni/Al_2O_3@Co_{500}, and Ni/Al_2O_3@Co_{600} with prolonged time when immersed in TC solution under light irradiation. (c) Variation in (e) surface temperature and (f) water mass of different systems of wet catalyst Ni/Al_2O_3@Co_{500} films with different shapes soaked in a TC solution with prolonged time under light conditions.

4. Conclusions

In summary, we constructed hydrangea-shaped Ni/Al_2O_3@Co nanoreactors *via in situ* polymerization of Co-incorporated dopamine followed by carbonization at different temperatures. The Co nanoparticles can be densely distributed onto the nanosheet of the hydrangea, ensuring the high exposure and accessibility of active species. Due to the superior electrical conductivity and synergistic effects of multiple metals, the obtained nanoreactor showcased the great activation properties of PMS and the excellent catalytic degradation performance for TC and other pollutants. In the catalytic degradation process, the activation of PMS contributes to abundant free radical species including $OH^{\bullet}$, $^{\bullet}SO_4^-$, $^{\bullet}O_2^-$, and $^1O_2$, synergistically triggering the great catalytic performance, among which $^{\bullet}O_2^-$ plays a major role in the degradation process. The obtained powder catalysts were tactically integrated into the tailored sponge with different shapes *via* a hydrogel crosslinking approach, which can be directly used as monolith stirrer catalysts for mechanical stirring during the catalytic degradation process. Furthermore, the integrated monolith sponge can act as a monolith evaporator for solar-driven interfacial evaporators. It is worth noting that the evaporator consisting of $Ni/Al_2O_3@Co_{500}$ also shows excellent photothermal conversion performance, and the device significantly improves the evaporation rate of clean water, presenting excellent practical application potential. Thus, this research provides a viable and sustainable solution for environmental pollution control and water resource utilization.

Data availability

All data generated or analysed during this study are included in this published article and its ESI.†

Conflicts of interest

The authors declare no conflict of interest.

Acknowledgements

This work was financially supported by the China National Natural Science Foundation (21908085), Natural Science Foundation of Jiangsu Provincial (BK20241950), China Postdoctoral Science Foundation (2023M731422), and Science and Technology Plan School-enterprise Cooperation Industry-university-research Forward-looking project of Zhangjiagang (ZKYY2341). The present study was also supported by the Jiangsu Provincial Key Laboratory of Environmental Science and Engineering (No. JSHJZDSYS-202103).

References

1 Y. Amangelsin, Y. Semenova, M. Dadar, M. Aljofan and G. Bjørklund, *Antibiotics*, 2023, **12**, 440.
2 T. Krithiga, S. Sathish, A. A. Renita, D. Prabu, S. Lokesh, R. Geetha, S. K. R. Namasivayam and M. Sillanpaa, *Sci. Total Environ.*, 2022, **831**, 154808.
3 T. Jiang, B. Wang, B. Gao, N. Cheng, Q. Feng, M. Chen and S. Wang, *J. Hazard. Mater.*, 2023, **442**, 130075.
4 H. Wang, Y. Zou, T. Luo, M. Benouahmane, D. Zhou and F. Wu, *Sep. Purif. Technol.*, 2022, **298**, 121607.
5 H. Li, X. Qin, K. Wang, T. Ma and Y. Shang, *Sep. Purif. Technol.*, 2023, 125900.
6 D. Li, S. Zhang, S. Li, J. Tang, T. Hua and F. Li, *J. Cleaner Prod.*, 2023, **397**, 136468.
7 Y. Shi, D. Feng, S. Ahmad, L. Liu and J. Tang, *Chem. Eng. J.*, 2023, **454**, 140244.
8 P. Niu, C. Li, D. Wang, C. Jia, J. Zhao, Z. Liu, X. Zhang and L. Geng, *Appl. Surf. Sci.*, 2022, **605**, 154732.
9 X. Zheng, X. Niu, D. Zhang, M. Lv, X. Ye, J. Ma, Z. Lin and M. Fu, *Chem. Eng. J.*, 2022, **429**, 132323.
10 Z. Y. Guo, C. X. Li, M. Gao, X. Han, Y. J. Zhang, W. J. Zhang and W. W. Li, *Angew. Chem., Int. Ed.*, 2021, **60**, 274–280.
11 L. Zou, X. Zhu, L. Lu, Y. Xu and B. Chen, *J. Hazard. Mater.*, 2021, **419**, 126427.
12 L. Baharudin, N. Rahmat, N. H. Othman, N. Shah and S. S. A. Syed-Hassan, *J. CO_2 Util.*, 2022, **61**, 102050.
13 M. Ma, R. Yang, C. He, Z. Jiang, J.-W. Shi, R. Albilali, K. Fayaz and B. Liu, *J. Hazard. Mater.*, 2021, **401**, 123281.
14 Q. Wu, H. Zhang, C. Ma, D. Li, L. Xin, X. Zhang, N. Zhao and M. He, *Carbon*, 2021, **176**, 367–373.
15 Z. Xie, Y. Li, Z. Zhou, Q. Hu, J. Wu and S. Wu, *J. Mater. Chem. A*, 2022, **10**, 7099–7110.
16 W. Li, K. Qian, Z. Yang, X. Ding, W. Tian and D. Chen, *Appl. Catal., B*, 2023, **327**, 122451.
17 Z. Li, X. Xu, X. Sheng, P. Lin, J. Tang, L. Pan, Y. V. Kaneti, T. Yang and Y. Yamauchi, *ACS Nano*, 2021, **15**, 12535–12566.
18 Y. Zhou, T. Ding, M. Gao, K. H. Chan, Y. Cheng, J. He and G. W. Ho, *Nano Energy*, 2020, **77**, 105102.
19 A. A. Tessema, C.-M. Wu, K. G. Motora and S. Naseem, *Compos. Sci. Technol.*, 2021, **211**, 108865.
20 N. Keller, J. Ivanez, J. Highfield and A. M. Ruppert, *Appl. Catal., B*, 2021, **296**, 120320.
21 J. Chen, J. Xiao, Z. Lu, C. Wang and L. Zhang, *J. Alloys Compd.*, 2021, **865**, 158645.
22 Q. Feng, Y. Zeng, S. Lin, B. Huang and X. Li, *Appl. Surf. Sci.*, 2022, **587**, 152755.
23 G. Borand, N. Akçamlı and D. Uzunsoy, *Ceram. Int.*, 2021, **47**, 8044–8052.
24 Y. Wang, J. Bao, C. Zuo, G. Dong, X. Sheng, Y. Huang, Y. Zhang and Y. Zhou, *Appl. Organomet. Chem.*, 2023, **37**, e6935.
25 H. Chen, R. Zhang, H. Wang, W. Bao and Y. Wei, *Appl. Catal., B*, 2020, **278**, 119311.
26 B. Wu, Z. Li, Y. Zu, B. Lai and A. Wang, *Water Res.*, 2023, **246**, 120678.
27 Z. Huang, X. Zhang, Z. Zhu, Z. Guo, X. Wang, L. Zhu, G. Zhang, B. Liu and D. Xu, *Chem. Eng. J.*, 2024, **480**, 147883.

28 M.-P. Zhu, J.-C. E. Yang, X. Duan, S. Wang, D. D. Sun, B. Yuan and M.-L. Fu, *Chem. Eng. J.*, 2021, **409**, 128162.
29 W. Liao, C. Tang, H. Zheng, J. Ding, K. Zhang, H. Wang, J. Lu, W. Huang and Z. Zhang, *J. Catal.*, 2022, **407**, 126–140.
30 R.-P. Ye, Q. Li, W. Gong, T. Wang, J. J. Razink, L. Lin, Y.-Y. Qin, Z. Zhou, H. Adidharma and J. Tang, *Appl. Catal., B*, 2020, **268**, 118474.
31 A. Cárdenas-Arenas, A. Quindimil, A. Davó-Quiñonero, E. Bailón-García, D. Lozano-Castello, U. De-La-Torre, B. Pereda-Ayo, J. A. González-Marcos, J. R. González-Velasco and A. Bueno-López, *Appl. Catal., B*, 2020, **265**, 118538.
32 L. Zeng, Y. Wang, Z. Li, Y. Song, J. Zhang, J. Wang, X. He, C. Wang and W. Lin, *ACS Appl. Mater. Interfaces*, 2020, **12**, 17436–17442.
33 Z. Zhang, K. Feng and B. Yan, *Catal. Sci. Technol.*, 2022, **12**, 4698–4708.
34 C. Italiano, J. Llorca, L. Pino, M. Ferraro, V. Antonucci and A. Vita, *Appl. Catal., B*, 2020, **264**, 118494.
35 A. Thakur and A. Kumar, *Chemosphere*, 2023, 140608.
36 N. Li, J. Ye, H. Dai, P. Shao, L. Liang, L. Kong, B. Yan, G. Chen and X. Duan, *Water Res.*, 2023, **235**, 119926.
37 X. Wang, H. Gai, Z. Chen, Y. Liu, J. Zhang, B. Zhao, A. Toghan and M. Huang, *Mater. Today Energy*, 2020, **18**, 100497.
38 Y. Shang, Y. Ding, P. Zhang, M. Wang, Y. Jia, Y. Xu, Y. Li, K. Fan and L. Sun, *Chin. J. Catal.*, 2022, **43**, 2405–2413.
39 S. Yang, W. Zhang, M. Liu, H. Zhao, H. Lu, H. Li, Z. Guo, A. Yuan, J. Yang and J. Pan, *J. Environ. Chem. Eng.*, 2023, **11**, 109190.
40 Z. Li, H. Ma, L. Zang, D. Li, S. Guo and L. Shi, *Sep. Purif. Technol.*, 2021, **276**, 119355.
41 M. Mohinuzzaman, J. Yuan, X. Yang, N. Senesi, S.-L. Li, R. M. Ellam, K. M. Mostofa and C.-Q. Liu, *Sci. Total Environ.*, 2020, **720**, 137395.
42 H. Xie, Q. Li, M. Wang, Y. Feng and B. Wang, *J. Hazard. Mater.*, 2024, **469**, 133946.
43 X. Chen, J. Zhou, H. Yang, H. Wang, H. Li, S. Wu and W. Yang, *Chemosphere*, 2022, **287**, 132074.
44 A. Calderon-Cardenas, E. A. Paredes-Salazar and H. Varela, *ACS Catal.*, 2020, **10**, 9336–9345.
45 G. Qian, J. Chen, T. Yu, L. Luo and S. Yin, *Nano-Micro Lett.*, 2021, **13**, 1–13.
46 B. Sun, H. Lv, Z. Liu, J. Wang, X. Bai, Y. Zhang, J. Chen, K. Kan and K. Shi, *J. Mater. Chem. A*, 2021, **9**, 6335–6344.
47 F. Yang, Y. Lu, X. Dong, M. Liu, Z. Li, X. Wang, L. Li, C. Zhu, W. Zhang and C. Yu, *J. Hazard. Mater.*, 2022, **424**, 127647.
48 W. Wang, M. Chen, D. Wang, M. Yan and Z. Liu, *Sci. Total Environ.*, 2021, **772**, 145522.
49 Y. Guo, L. Yan, X. Li, T. Yan, W. Song, T. Hou, C. Tong, J. Mu and M. Xu, *Sci. Total Environ.*, 2021, **783**, 147102.
50 W. Tu, G. Wang, Y. Zhang, H. Zhu, R. Du, H. Zhao, S. Tang, Z. Guo, J. Yang, F. Yang and C. Zhu, *Rare Met.*, 2024, **43**, 3146–3160.
51 H. Zhu, M. Liu, G. Wang, R. Du, H. Zhao, H. Lu, S. Yang, S. Tang, Z. Guo, J. Yang, C. Zhu and F. Yang, *Rare Met.*, 2024, **43**, 1686–1701.
52 H. Zhao, D. Shang, H. Li, M. Aizudin, H. Zhu, X. Zhong, Y. Liu, Z. Wang, R. Ni, Y. Wang, S. Tang, E. H. Ang and F. Yang, *Mater. Horiz.*, 2024, **11**, 5081–5093.
53 H. Zhu, R. Du, H. Zhao, M. Liu, Y. Wang, C. Yu, Z. Guo, S. Tang, E. H. Ang and F. Yang, *J. Mater. Chem. A*, 2024, **12**, 8487–8501.
54 H. Li, M. Aizudin, S. Yang, Z. Guo, J. Yang, F. Yang, E. H. Ang and J. Pan, *Sep. Purif. Technol.*, 2023, **326**, 124802.